
Article:
Li, J., Zhu, X-K., Bowyer, F.T. et al. (2026) A molybdenum isotope perspective on oceanic palaeoredox conditions during the Cryogenian non-Snowball interlude. Global and Planetary Change, 263. 105526. ISSN: 0921-8181

https://doi.org/10.1016/j.gloplacha.2026.105526

A molybdenum isotope perspective on oceanic palaeoredox conditions during the Cryogenian non-Snowball interlude

Jin Li[a], Xiang-kun Zhu[a,b]*, Fred T. Bowyer[c,d], Benjamin J. W. Mills[c], Xi Peng[a], Bin Yan[a], Simon W. Poulton[c]

[a]*MNR Key Laboratory of Isotope Geology, Institute of Geology, Chinese Academy of Geological Sciences, Beijing, Chin*

[b]*State Key Laboratory of Deep Earth and Mineral Exploration*

[c]*School of Earth, Environment and Sustainability, University of Leeds, Leeds, LS2 9JT, UK*

[d]*School of GeoSciences, University of Edinburgh, Edinburgh, EH9 3FE, UK*

** Corresponding author. e-mail: xiangkun@cags.ac.com*

Phone number: 8613911753121

Fax number: 861068999798

Abstract

The Cryogenian Period included at least two long-lived global Snowball glaciations, the Sturtian and Marinoan, which were separated by a non-Snowball interval that lacks evidence for persistent ice cover. Non-Snowball Cryogenian sediments record the earliest possible rise of chlorophyte algae, high magnitude perturbations to the carbon cycle, and possible evidence for a substantial increase in atmospheric oxygen. The shallow marine Datangpo Formation and the correlative, deep-marine Xiangmeng Formation document continuous, shale-dominated sequences that were deposited in the Nanhua Basin on the Yangtze Craton (South China) during the non-Snowball interval. Previous studies have extrapolated estimates of seawater molybdenum isotope (δ^{98}Mo) compositions for the non-Snowball using data from the lower Datangpo Fomation and the Arena Formation of east Greenland, which either constitute only a small portion of the total thickness of non-Snowball deposits, or are difficult to assess based on the likelihood of isotopic fractionation during non-quantitative Mo drawdown. To address these limitations, we report bulk rock Fe speciation data in combination with published redox sensitive trace element (Mo and U) concentration data from euxinic marine sedimentary rocks that were deposited throughout the non-Snowball interval. Local syn-depositional and diagenetic effects during Mn-carbonate precipitation are considered during interpretations of regional

redox datasets, and these insights provide a base framework for the robust interpretation of new δ^{98}Mo data from euxinic sediments. The result is a better constrained and continuous record of global ocean palaeoredox change throughout the non-Snowball interval. The global Mo dataset shows an increase in δ^{98}Mo from +0.67 ± 0.06‰ to +1.12 ± 0.09‰, and a contemporaneous decrease in maximum Mo concentrations in euxinic sediments. Using these data, we employ a single reservoir model to evaluate the evolving spatial extent of different oceanic redox states. When assuming a post-Sturtian decrease in weathering input, the model results suggest that substantial anoxic seafloor was maintained throughout the non-Snowball, while euxinic seafloor area decreased, mirroring trends in regional redox proxy data. Our geochemical data and modelling further support the proposal that both temperature and redox conditions in marine environments may have been more hospitable in the latter part of the non-Snowball interlude, broadly contemporaneous with the earliest possible evidence for the emergence of animal life.

Keywords: Cryogenian; Mo isotopes; Nanhua Basin; palaeoredox; non-Snowball

1. Introduction

The Cryogenian Period encapsulates at least two 'Snowball Earth' glaciations (Hoffman et al., 1998, 2017): the Sturtian (ca. 717–661 Ma) and Marinoan (ca. ≤651–635Ma), when ice sheets extended to sea level at low latitudes for millions of years (Wang et al, 2019; Zhou et al., 2020; Condon et al., 2005; Lan et al., 2014, Bao et al. 2018; Rooney et al., 2020; Ma et al., 2023; Tasistro-Hart et al., 2025). The intervening mid-Cryogenian 'non-Snowball' interval (ca. 661 Ma to ≥640 Ma) is represented by globally widespread marine deposition, but intermittent glacial deposition may have persisted in some successions (e.g., Oman, Allen et al., 2011), and so the term 'non-glacial' is avoided. The Sturtian and Marinoan separate the generally single-celled and morphologically simple eukaryotes of the preceding Proterozoic fossil record, from the morphologically complex multi-celled eukaryotes and metazoans of the succeeding Ediacaran Period (e.g., Xiao and Tang, 2018), although multicellular red algae in particular had already evolved by the earlier Proterozoic (e.g., Zhu et al., 2016). Cryogenian non-Snowball sedimentary rocks may also preserve molecular biomarker evidence for a significant increase in the contribution of chlorophyte (green) algae to the biomass produced through marine primary production, alongside the earliest putative biomarker evidence for sponge-grade animals (Love et al., 2009; Brocks et al., 2017, but see Brocks et al., 2023). The possible proliferation of green algae at this time has been linked to a combination of nutrient delivery to the oceans and gradual global cooling following the inhospitable super-greenhouse conditions that immediately followed Sturtian deglaciation (Brocks et al., 2017; Bowyer et al., 2023).

Reconstructing marine redox chemistry during the Cryogenian is crucial for understanding the potential relationships between environmental conditions, the rise of green algae and the possible emergence of early animals. To this end, numerous studies have explored marine paleoredox conditions by analyzing mid-Cryogenian marine shale-dominated successions. These include the Datangpo Formation in South China (e.g., Li et al., 2012; Zhang et al., 2015; Bowyer et al., 2023), the MacDonaldryggen Member of the Elbobreen Formation in Svalbard (Canfield et al., 2008; Kunzmann et al., 2015), the Tapley Hill Formation and the Aralka Formation in Australia (Canfield et al., 2008; Bowyer et al., 2023), the Twitya Formation in NW Canada (Sperling et al., 2015), and the Arena Formation in East Greenland (Canfield et al., 2008; Scheller et al., 2018). The available data suggest that, while individual depositional environments were characterized by continued water column redox stratification throughout the non-Snowball interval, many regions experienced approximately isochronous shifts in the Sturtian aftermath, from euxinic through ferruginous to possible oxic shallow marine conditions (e.g., compilation of Bowyer et al., 2023 and references therein). In order to better understand how regional palaeoredox conditions from sedimentary rocks deposited in shelf-to-slope environments relate to global-scale changes in the spatial extent of oxygenated bottom

waters, it is necessary to investigate the isotopic composition of redox sensitive elements that have long mean oceanic residence times, such as δ^{98}Mo and δ^{238}U (e.g., Dahl et al., 2011; Lau et al., 2017).

Despite more than two decades of extensive research, the evolution of global marine redox conditions during the non-Snowball interval remains a subject of ongoing debate. Lau et al. (2017) reported relatively high δ^{238}U values from limestones of the lower Taishir Group in Mongolia, and interpreted these data as evidence for a short-lived post-Sturtian global oxygenation event. Similarly, Zhang et al. (2015) documented positive δ^{56}Fe values in basal black shales of the Datangpo Formation, followed by a shift toward values typical of riverine inputs in the middle part of the succession. This trend was also interpreted to reflect a transient oxygenation episode followed by a return to anoxic conditions in the Nanhua Basin. By contrast, previous studies that analysed δ^{98}Mo of organic-rich black shales from the lower Datangpo Formation deposited in open slope settings (e.g., Chen et al., 2015; Cheng et al., 2018) suggested that widespread anoxia prevailed during the non-Snowball interval. However, these latter studies extrapolated seawater δ^{98}Mo for the entire non-Snowball interval using data from only the lower Datangpo Formation, where proxy records may be at least partially confounded by extensive Mn-carbonate deposition and associated local Mo isotope fractionation. The lower Datangpo Formation also constitutes only a small portion of the total thickness of the regional non-Snowball succession. At present, the potentially-conflicting interpretations from these isotopic datasets preclude a comprehensive understanding of global environmental change and possible evolutionary responses during this critical interval.

Here, we investigate local and global paleoredox dynamics using an integrated analysis of δ^{98}Mo, Fe speciation, and redox sensitive trace element (RSE) concentration data. We target two drill cores (Daotuo and Xiangtan sections) that constitute continuous sequences of black shale, Mn-carbonate, grey shale and grey siltstone spanning the entire Cryogenian non-Snowball interval in South China. We then combine our best estimates of seawater δ^{98}Mo and Mo concentrations ([Mo]), incorporating existing δ^{98}Mo datasets from other Cryogenian non-Snowball sequences, to calibrate a single reservoir model and to better constrain long-term trends in global ocean paleoredox conditions throughout the mid-Cryogenian.

2. Geological setting and sampling strategy

The Cryogenian Yangtze Platform can be sub-divided into three broad depositional environments based on distinct lithofacies groupings. From northwest to southeast, these include: (1) upper slope facies; (2) lower slope facies; and (3) basin facies (Bao et al., 2018; Fig 1). As a fault-bounded rift basin, the Nanhua Basin was probably semi-restricted, with some smaller scale bathymetric complexity resulting in occasional separation of local depositional

environments from the open ocean by marginal sills (Wang and Li, 2003; Li et al., 2012). Regional reconstructions reveal a series of NE-SW-trending horsts and grabens across the study area that are likely to have produced multiple, internal sub-basins with varying degrees of water mass restriction (Du et al., 2015). Cheng et al. (2018) suggested that the Datangpo Formation was deposited in a silled basin that gradually evolved into a semi-restricted basin, and salinity reconstructions (Cheng et al., 2021; Wei et al., 2024) support repeated seawater influx into a semi-closed basin. Ultimately, the extent to which waters from the basin mixed with the open ocean is not well constrained and was likely temporally variable, but most paleogeographic and regional tectonic reconstructions, alongside reconstructed variability in palaeosalinity data, suggest that the basin may have been at least intermittently connected to the open ocean to the northeast and southwest (Wang and Li, 2003).

The Datangpo and Xiangmeng formations are continuous, time-equivalent, siliciclastic-dominated successions that were deposited in the Nanhua Basin during the Cryogenian non-Snowball interval (Zhang et al., 2015; Bao et al., 2018; Peng et al., 2019) (Fig. 1). These two formations are sandwiched between two prominent and spatially extensive glacial diamictites; the older Tiesi'ao Formation (also named the Gucheng Formation in western Hunan Province) and the younger Nantuo Formation (Zhang et al., 2008; Peng et al., 2019). The thickness of the Datangpo Formation varies from <130 m in shelf areas to >500 m in lower slope settings (Wang and Li, 2003). Here, we present data from two drill cores comprising the Daotuo (core ZK105, documenting the Datangpo Formation) and the Xiangtan (core ZK3603, documenting the Xiangmeng Formation) sections. The detailed lithostratigraphy of these sections has been described by Zhang et al. (2015) and Peng et al. (2019).

The Daotuo section represents continuous open-slope deposition in the Nanhua Basin, and comprises (from bottom to top): ca. 1 m of black shale, ca. 3.45 m of thin-bedded black Mn-carbonate, ca. 19.35 m of organic-rich black shale with rare Mn-carbonate interbeds, ca. 38 m of black shale, ca. 139 m of grey shale, and ca. 9 m of grey siltstone. In the Daotuo section, the Datangpo Formation is overlain without notable depositional hiatus by the Marinoan-equivalent Nantuo glacial diamictite (Zhang et al., 2015; Peng et al., 2019). The studied part of the Daotuo section can be sub-divided into 3 members that broadly shallow-up and exhibit distinct bulk lithofacies (Figs. 1 and 2). Member I is a 51.3 m-thick interval composed of black shales and organic-rich Mn-carbonate layers, Member II is a 145 m-thick grey shale, and Member III is a 52.5-m-thick grey siltstone.

The Xiangtan section records continuous deposition in a deeper marine setting and comprises 0.04 m of Mn-carbonate overlain by ca. 87.5 m of organic-rich black shale. This transitions without notable depositional hiatus into the Marinoan-age diamictite of the Nantuo Formation (Peng et al., 2019). The Tie'siao/Gucheng and Nantuo diamictite deposits were deposited during the Sturtian and Marinoan Snowball Earth events, respectively (Condon et al., 2005;

Zhu et al., 2007; Zhang et al., 2008; Wang et al., 2019). Thus, the Datangpo and Xiangmeng formations each span the entire non-Snowball interval (Peng et al., 2019). Based on lithostratigraphy, grain size analysis and inferred rates of sedimentation, the Datuo section is interpreted to have been deposited in a shallower shelf setting than the Xiangtan section (Bao et al., 2018; Peng et al., 2019).

Zircon U-Pb ages from ash beds in the Datangpo Formation suggest that deposition commenced at ca. 661 Ma (e.g., Rooney et al., 2020) and continued until later than 651.2 ± 3.3 Ma (Ma et al., 2023). The available ages are consistent with both short (ca. 11 Myr) and long (ca. 20 Myr) duration models for the non-Snowball interlude (e.g., Bowyer et al., 2023; Tasistro-Hart et al., 2025).

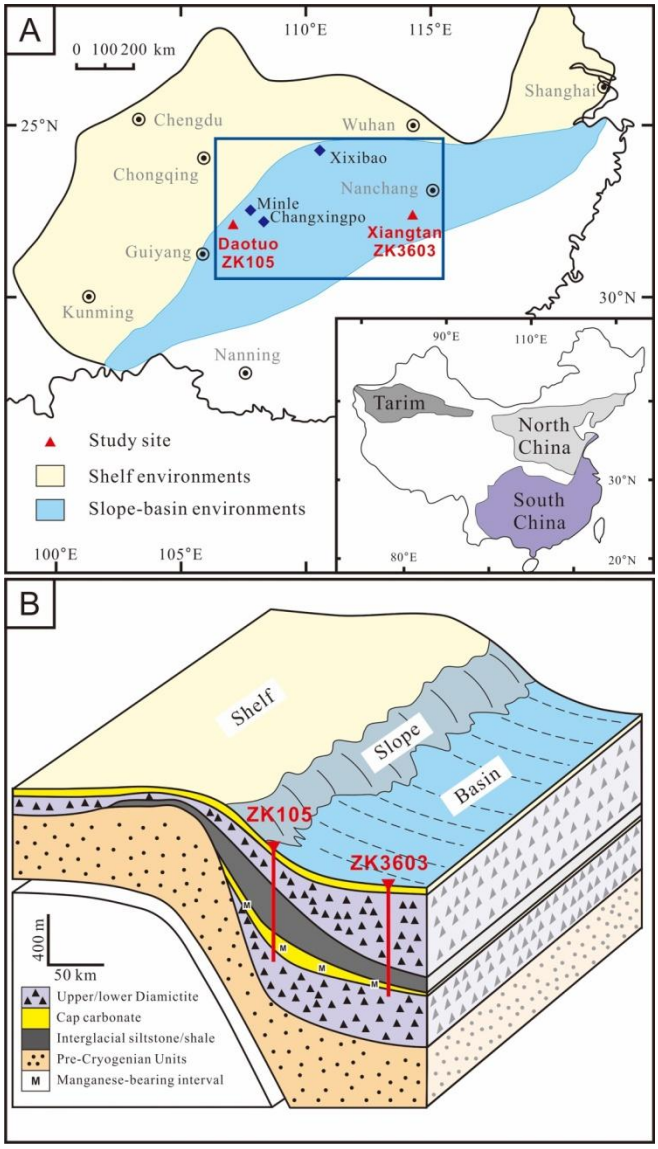

Fig. 1. Simplified palaeogeographic map of the study area (Peng et al., 2019). **(A)** Generalized Cryogenian paleogeographic reconstruction of South China. **(B)** Simplified bathymetric reconstruction showing the relative paleodepths of the studied sections.

3. Analytical methods

3.1 Major and trace elements

The major and trace element data reported here are from bulk rock analyses of Zhang et al. (2015) for the Daotuo section (Table S1), and Shi et al. (2016) for the Xiangtan section (Table S2). To assess and compare the authigenic fractions of RSEs, enrichment factors (EFs) for siliciclastic samples were calculated as $X_{EF} = [(X/Al)_{sample}/(X/Al)_{UCC}]$ (Tribovillard et al., 2006; Algeo and Tribovillard, 2009), while those for carbonate samples were calculate as $X_{EF}* = [(X_{sample} – (Al_{sample} * (X/Al)_{UCC})) + X_{UCC}]/X_{UCC}$ (Krewer et al., 2024), where X and Al represent the concentrations of RSEs and Al, respectively. Data are normalized to average upper continental crust (UCC) concentrations (McLennan, 2001). For comparison, Table S3 also presents enrichment factor data that were calculated using UCC compositions after Rudnick and Gao (2003).

3.2. Iron speciation

Iron speciation analyses were performed in the Cohen Laboratories, University of Leeds, following the sequential extraction methods of Poulton and Canfield (2005). Total Fe (Fe_T) was determined on ashed samples via digestion with HF-HNO_3-$HClO_4$. Carbonate-associated iron (Fe_{carb}), ferric (oxyhydr)oxides (Fe_{ox}), and magnetite (Fe_{mag}) were sequentially leached with Na-acetate, Na-dithionite and ammonium oxalate, respectively (Poulton and Canfield, 2005). Iron concentrations from the total digests and the sequential extractions were measured by atomic absorption spectroscopy. Pyrite (Fe_{py}) was determined separately by chromous chloride distillation (Canfield et al., 1986). The combination of Fe_{carb}, Fe_{ox}, Fe_{mag} and Fe_{py} defines an Fe pool that is considered highly reactive (Fe_{HR}) towards abiological reduction under anoxic conditions. The Fe speciation reference material, WHIT (Alcott et al., 2020), was run alongside the samples to ensure quantitative extractions. Our results are in close agreement with certified values, with relative standard deviations of <5% for all stages. Data for the Daotuo section are listed in Table S1, while data for the Xiangtan section are from Bowyer et al. (2023) and are reported in Table S2.

3.3. Mo isotopes

Mo isotopes ($\delta^{98}Mo$) were analyzed following the methods described by Li et al. (2016). Approximately 0.5–1.0 g of powdered sample (giving 0.2–0.5 μg of Mo) was accurately weighed into 50 ml quartz crucibles and ashed at 600°C for 6 h in a muffle furnace to decompose the organic materials. After cooling, the samples were transferred to 15 ml Savillex beakers, where a ^{100}Mo-^{97}Mo double spike solution was added to produce a $^{100}Mo_{spike}/^{100}Mo_{sample}$ ratio

of ca. 3. Samples were then digested using 8 ml of concentrated HCl on a hot plate at 130°C for approximately 1 day. The sample solutions were then centrifuged for 5 min at 4000 rpm to separate the leachates from residual solids (Li et al., 2022). The leachates were evaporated to dryness and then dissolved in 7 ml of 1 M HF/0.5 M HCl and centrifuged for 5 min at 4000 rpm to remove residual solids. The chromatographic procedure used 2 ml of Bio-Rad AG® 1-X8 anion exchange resin in a 10-ml Poly-Prep® column. All Mo isotopic measurements were carried out in the Laboratory of Isotopic Geology, Institute of Geology, Chinese Academy of Geological Sciences (Beijing), using a Nu Plasma HR type MC-ICP-MS equipped with a Nu Instruments DSN-100 desolvating nebulizer (in dry mode; see Supplementary Table S4 for details of the operating parameters). The Mo isotope data were normalized following Nägler et al. (2014) in per mil notation, where the δ^{98}Mo composition of NIST SRM 3134 (Lot No. 891307) was set to 0.25‰, defined as:

$$\delta^{98}\text{Mo}\ (‰) = (((^{98}\text{Mo}/^{95}\text{Mo})_{\text{sample}}/((^{98}\text{Mo}/^{95}\text{Mo})_{\text{NIST 3134}} - 1) \times 1000 + 0.25$$

To assess accuracy, we measured the δ^{98}Mo composition of the USGS reference material SGR-1b, with replicate analyses giving a value of 0.69 ± 0.08‰ (relative to the certified value of 0.69 ± 0.06‰; Gaspers et al., 2020), while our CAGS-BS laboratory reference material yielded a value of 0.10 ± 0.02‰ (relative to the long-term laboratory value of 0.15 ± 0.07‰).

4. Results

The Fe speciation and Mo isotope data obtained in this study, as well as accompanying geochemical data published previously for the Daotuo and Xiangtan sections (Zhang et al., 2015; Shi et al., 2016; Bowyer et al. 2023), are summarized in Figs. 2 and 3. The data reveal distinct stratigraphic patterns in Mo and U distributions through the studied sections. In the Daotuo section, Member I shales are commonly (but not always) enriched in Mo (0.22–36.2 μg/g; mean = 7.4 μg/g, Fig. 2D), giving Mo_{EF} values of 0.13 to 24.1 (Fig. 2F). This contrasts with the relatively uniform U concentrations (2.06–4.41 μg/g; mean = 2.83 μg/g, Fig. 2E) and moderate U_{EF} values (0.57–1.18) (Fig. 2G). Mn-carbonate samples in Member 1 tend to have low to intermediate Mo (0.08–7.69 μg/g; mean = 1.49 μg/g, Fig. 2D) and low U concentrations (0.29–2.94 μg/g; mean = 1.38 μg/g, Fig. 2E). These result in Mo_{EF}* values that are of generally lower magnitude than those of interbedded shales, in the range 0.72–5.50 (mean = 1.61, Fig. 2F). By contrast, U_{EF}* values in the range 1.03–1.11 are similar to the surrounding black shale samples (Fig. 2G). Siliciclastic samples throughout Members 2 and 3 show far lower Mo concentrations (0.17–0.94 μg/g, mean = 0.34 μg/g, Fig. 2D) and U concentrations (2.06–2.81 μg/g, mean = 2.35 μg/g), resulting in enrichment factor values for Mo and U that are ubiquitously less than 1. The Xiangtan shales generally have relatively low Mo (0.83–3.79 μg/g; Mo_{EF} = 0.68–3.21)

and U contents (1.62–4.22 μg/g; U_{EF}=0.73–1.49), but samples with both Mo and U enrichment factors >1 are found towards the top of the Xiangmeng Formation between ca. 490 m and 480 m depth (Fig. 3).

Iron speciation is widely used to investigate the local to regional redox state of ocean basins (Poulton and Canfield, 2005; 2011). Calibration of the iron speciation proxy in modern and ancient sediments demonstrates that Fe_{HR}/Fe_T <0.22 is commonly indicative of deposition under oxic conditions (Poulton and Canfield, 2011). By contrast, Fe_{HR}/Fe_T >0.38 commonly occurs due to accumulation of Fe_{HR} minerals under anoxic water column conditions (Raiswell and Canfield, 1998). Where anoxic depositional conditions are inferred from Fe_{HR}/Fe_T >0.38, Fe_{py}/Fe_{HR} may be used to differentiate ferruginous (<0.6) from possibly euxinic (>0.6) conditions (Poulton and Canfield, 2011; Benkovitz et al., 2020; Poulton, 2021).

In the Daotuo section, Fe_T ranges from 0.73–7.88 wt% (mean = 5.18 wt%), and Fe_{HR}/Fe_T and Fe_{py}/Fe_{HR} ratios show some stratigraphic variability (Figs. 2A and 2B). In Member I, Fe_{HR}/Fe_T ratios range from 0.09–0.91 (mean = 0.55), but the majority of samples have ratios >0.38, with the exception of three samples in the upper part of Member I (Fig. 2A). Fe_{py}/Fe_{HR} ratios range from 0.11–0.78 (mean = 0.54), with most samples falling between 0.6–0.8 (Fig. 2B). Importantly, the observed decrease in Fe_{HR}/Fe_T does not correlate with a notable transition in dominant lithology from interbedded black shales and organic-rich Mn-carbonate layers to black shales through Member I, supporting a primary water column signature rather than a trend that purely reflects changing lithology or depositional rate. Samples from members II and III of the Daotuo section have Fe_{HR}/Fe_T ratios <0.38, in the range of 0.04–0.32 (mean = 0.19) (Fig. 2A). In the Xiangtan section, Fe_T ranges from 2.23–4.09 wt% (mean = 2.93 wt%) and samples show persistent enrichments in Fe_{HR}, demonstrated by Fe_{HR}/Fe_T >0.60 (range = 0.64–0.82, mean = 0.74), with Fe_{py}/Fe_{HR} ratios that are commonly elevated (range = 0.48–0.88, mean = 0.68; Figs. 3A and 3B).

The δ^{98}Mo compositions of samples from the Daotuo section range from −2.23 to +1.31‰ (-0.08 ± 1.57‰). Values for δ^{98}Mo in Mn-carbonate samples range from +0.32 to +1.03‰ (+0.56 ± 0.49‰), whereas black and grey shale samples range from −1.21 to +1.31‰ (+0.24 ± 1.15‰) and −2.23 to −0.02‰ (−0.99 ± 1.13‰), respectively. Siltstone samples range from +0.08 to +0.22‰ (+0.13 ± 0.13‰) (Fig. 2I). However, up-core changes in δ^{98}Mo compositions through Member I do not correlate with notable changes in dominant lithology. The δ^{98}Mo compositions of black shales from the Xiangtan section range from −1.07 to +1.28‰ (+0.66‰ ± 0.90). In the Xiangtan section, samples with Fe_{HR}/Fe_T >0.38 and Fe_{py}/Fe_{HR} >0.60 can be divided into a lower interval (570–510.5 m) where δ^{98}Mo values remain relatively constant (in the range +0.75 to +0.81‰), and an upper interval (508.5–482 m) where δ^{98}Mo has greater variability (in the range −0.65 to +1.28‰; Fig. 3H).

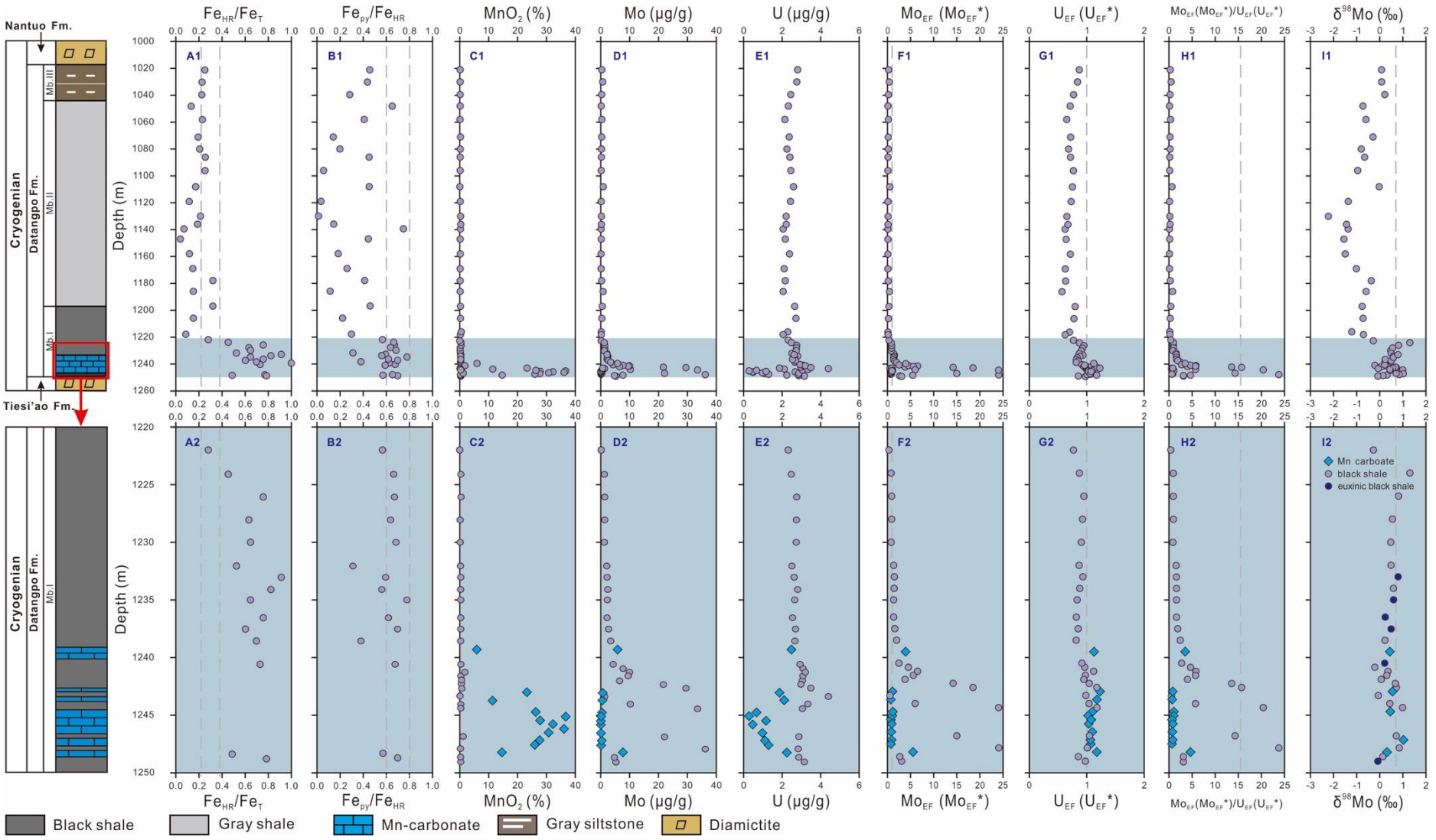
Nantuo Fm.
Cryogenian
Datangpo Fm.
Mb.III
Mb.II
Mb.I
Tiesi'ao Fm.
Depth (m)
A1
B1
C1
D1
E1
F1
G1
H1
I1
A2
B2
C2
D2
E2
F2
G2
H2
I2
Mn carboate
black shale
euxinic black shale
Black shale
Gray shale
Mn-carbonate
Gray siltstone
Diamictite

235

Fig. 2. Geochemical data for the Daotuo section. (A) Fe_{HR}/Fe_T, (B) Fe_{py}/Fe_{HR}, (C) MnO_2 concentrations (wt%), (D) Mo concentrations (μg/g), (E) U concentrations (μg/g), (F) Mo_{EF}, (G) U_{EF}, (H) Mo_{EF}/U_{EF} ratios, and (I) $\delta^{98}Mo$ (‰). Circles represent shale samples and diamonds represent carbonate samples. Vertical dashed lines in Fig. 2A correspond to calibrated thresholds for anoxic ($Fe_{HR}/Fe_T \geq 0.38$) and oxic ($Fe_{HR}/Fe_T \leq 0.22$) deposition (Poulton and Canfield, 2011). Vertical dashed lines in Fig. 2B correspond to calibrated thresholds for possibly euxinic ($Fe_{py}/Fe_{HR} > 0.6$) and euxinic ($Fe_{py}/Fe_{HR} > 0.8$) deposition (Poulton, 2021). Figs. 2A1-I1 show the full core data, and Figs. 2A2-I2 show an expanded view of the lower part of Member I (from the bottom of Datangpo Formation to 1222 m). In panel I2, data are distinguished based on lithology (Mn carbonate-rich samples vs siliciclastic samples) and euxinic black shales are also distinguished from oxic/anoxic, non-sulfidic siliciclastic samples based on a combination of Fe speciation ($Fe_{HR}/Fe_T > 0.38$, $Fe_{py}/Fe_{HR} > 0.6$) and RSE enrichment factors (>1). Enrichment factors were calculated using UCC compositions of McLennan (2001).

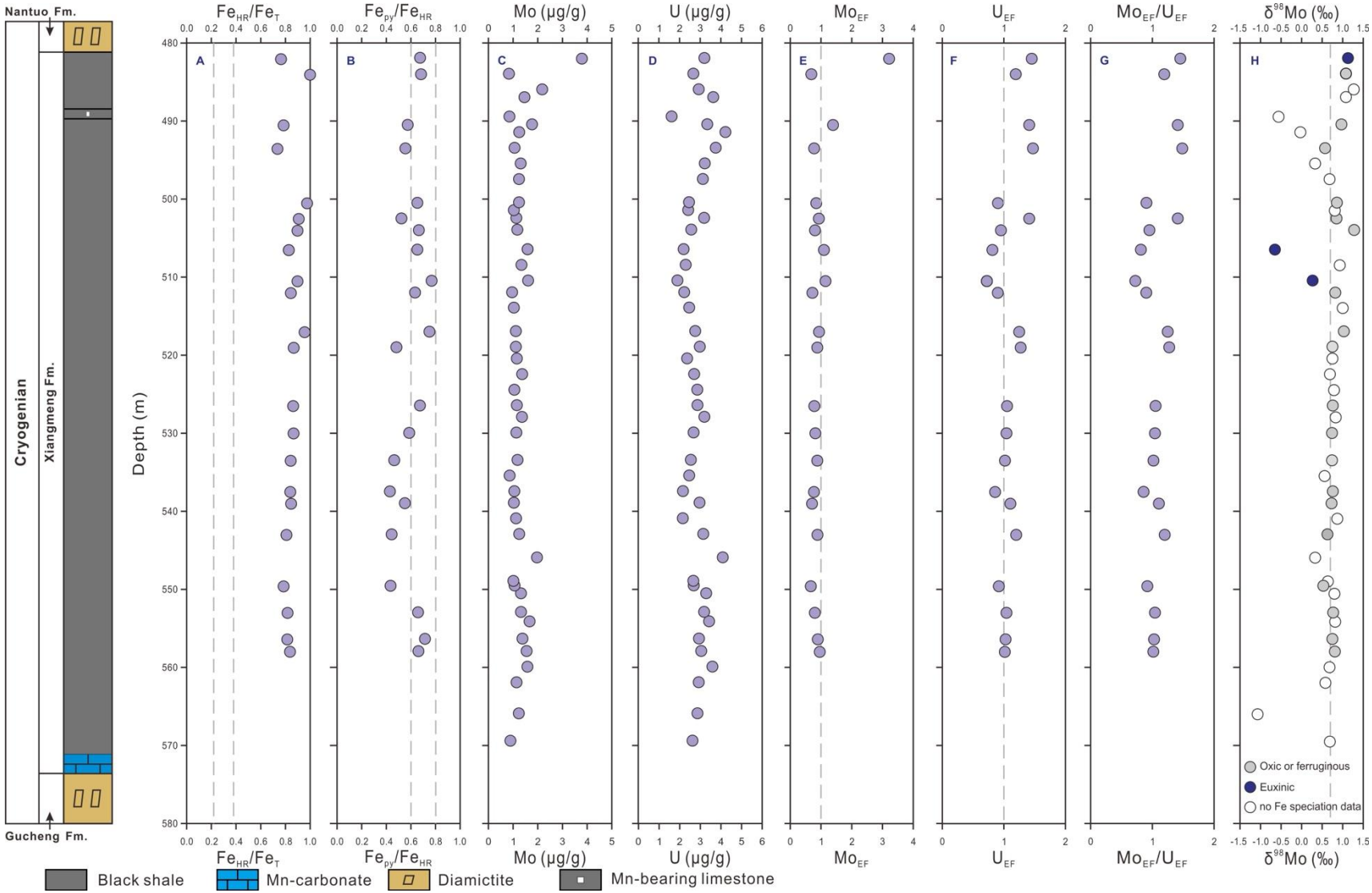
Nantuo Fm.
Cryogenian
Xiangmeng Fm.
Gucheng Fm.
Depth (m)
A
B
C
D
E
F
G
H
Oxic or ferruginous
Euxinic
no Fe speciation data
Black shale
Mn-carbonate
Diamictite
Mn-bearing limestone

244

Fig. 3. Geochemical data for the Xiangtan section. (A) Fe_{HR}/Fe_T, (B) Fe_{py}/Fe_{HR}, (C) Mo concentrations (μg/g), (D) U concentrations (μg/g), (E) Mo_{EF}, (F) U_{EF}, (G) Mo_{EF}/U_{EF} ratios, (H) δ^{98}Mo (‰) for all samples, and (I) δ^{98}Mo (‰) for euxinic shales only (note that error bars for isotopic analyses are within the size of the symbols). Vertical dashed lines in Fig. 3A correspond to calibrated threshold ratios for anoxic ($Fe_{HR}/Fe_T \geq 0.38$) and oxic ($Fe_{HR}/Fe_T \leq 0.22$) deposition (Poulton and Canfield, 2011). Vertical dashed lines in Fig. 3B correspond to calibrated threshold ratios for possibly euxinic ($Fe_{py}/Fe_{HR} > 0.6$) and euxinic ($Fe_{py}/Fe_{HR} > 0.8$) deposition (Poulton, 2021). Data filtering in panel H reflects lithology (Mn-carbonate vs. black shale) and paleoredox interpretations based on a combination of Fe speciation ($Fe_{HR}/Fe_T > 0.38$, $Fe_{py}/Fe_{HR} > 0.6$) and RSE enrichment factors (>1). Enrichment factors were calculated using UCC composition of McLennan (2001).

5. Discussion

5.1. Controls on Mo isotopic composition during the Cryogenian

The residence time of Mo in the Cryogenian ocean (estimated to be ca. 100–200 kyr) was likely shorter than it is today (ca. 440 kyr) because of the relatively small global oceanic Mo reservoir arising from drawdown of Mo to sediments under widespread anoxic water column conditions, alongside a low influx from relatively subdued oxidative weathering (e.g., Siebert et al., 2003; Asael et al., 2018; Scheller et al., 2018). Nevertheless, the residence time of Mo likely still greatly exceeded the oceanic mixing time (ca. 1.5 kyr) (Sarmiento and Gruber, 2006; Dahl et al., 2011; Miller et al., 2011). Indeed, mass balance models suggest that the Neoproterozoic ocean was well-mixed with respect to Mo, and thus estimates for the δ^{98}Mo composition of seawater based on euxinic sediments, if deposited in settings that were at least temporarily unrestricted from the global ocean and unaffected by other local fractionation effects (see below), should approximate the global seawater value (Dahl et al., 2011; Scheller et al., 2018).

The upper continental crust has an average δ^{98}Mo composition of +0.3 to +0.4‰ (Voegelin et al., 2014). Adsorption of Mo onto Mn (oxyhydr)oxides (MnO_x) results in significant isotopic fractionation ($\Delta^{98}Mo_{MnOx\text{-}seawater} = \delta^{98}Mo_{MnOx} - \delta^{98}Mo_{seawater}$ = -3‰; Barling et al., 2004), while Mo adsorption onto Fe (oxyhydr)oxides (Fe_{OX}) results in variable fractionation factors depending on the precise Fe mineralogy ($\Delta^{98}Mo_{Fe\ OX\text{-}seawater} = \delta^{98}Mo_{Fe\ OX} - \delta^{98}Mo_{seawater}$ = -0.83 to -2.19 ‰; Goldberg et al., 2009). Non-quantitative Mo drawdown under anoxic, non-euxinic to weakly euxinic conditions may also result in significant isotopic fractionation (Poulson et al., 2006; Poulson Brucker et al., 2009). When dissolved Mo is not quantitatively removed, the sediments exhibit lower δ^{98}Mo values compared to global seawater, while the overlying bottom waters become enriched in isotopically heavy Mo (Nägler et al., 2011; Noordmann et al., 2015). When bottom waters are intermittently euxinic or contain low $[H_2S]_{aq}$ (<11 μM), a wide range of δ^{98}Mo compositions (–0.6 to +1.8‰) may be observed in the underlying sediments, likely reflecting the slow and incomplete conversion of molybdate to thiomolybdate (Arnold et al., 2004; Nägler et al., 2005; Neubert et al., 2008; Dahl et al., 2010, Noordmann et al., 2015).

Overall, the isotopic composition of Mo in anoxic sediments deposited from mildly oxygenated to anoxic (but non-euxinic) bottom waters depends on a number of factors, including the concentrations of Fe and Mn (oxyhydr)oxides and their precise mineralogy, as well as the availability of dissolved H_2S in sediment pore waters (Poulson Brucker et al., 2009; Goldberg et al., 2009; 2012). Goldberg et al. (2012) identify three fractionation groups: 1) Mn-rich sediments with low dissolved porewater H_2S (δ^{98}Mo = –

1.0 to + 0.4‰); 2) Fe-rich sediments with low dissolved porewater H_2S ($\delta^{98}Mo$ = –0.5 to + 2.0‰); and 3) sediments with high dissolved porewater H_2S concentrations ($\delta^{98}Mo$ = 1.6 ± 0.2‰). These variable isotopic fractionations arise, at least in part, due to a fractionation of ca. 0.9‰ during Mo-sulfide precipitation (Poulson Brucker et al., 2012). However, under strongly euxinic conditions (H_2S concentrations above 11 μmol L^{-1}), molybdate may be quantitatively transformed into thiomolybdate (MoS_4^{2-}) with negligible isotopic fractionation (Helz et al., 1996; Nägler et al., 2011). Mo isotope systematics thus provide a powerful tool for tracing the spatial extent of different redox conditions on a global scale, assuming that regional depositional paleoredox conditions are accurately distinguished (Kendall et al., 2017).

5.2. Bottom water redox conditions in the Nanhua Basin

In the Daotuo section, black shales from lower Member I have Fe_{HR}/Fe_T >0.38, with the majority of samples yielding Fe_{py}/Fe_{HR} >0.6 (Fig. 2B). By contrast, black shales from upper Member I, grey shales from Member II, and grey siltstones from Member III all yield Fe_{HR}/Fe_T <0.38, with Fe_{py}/Fe_{HR} ratios that fluctuate considerably, but with most values being <0.6 (note that the Fe_{py}/Fe_{HR} proxy for identifying water column euxinia is only valid for samples that show independent evidence for deposition under anoxic conditions; Poulton and Canfield, 2011; Poulton, 2021). Elevated Fe_{HR}/Fe_T and Fe_{py}/Fe_{HR} ratios, alongside moderate to high Mo enrichments, in the lower part of Member I suggest short-lived intervals of euxinia in the Daotuo section, in agreement with previous studies of the Datangpo Formation in other sections (e.g., Li et al., 2012; Zhang et al., 2015; Cheng et al., 2018; Peng et al. 2019; Bowyer et al., 2023). Of the twelve samples from the Daotuo section with Fe speciation data that suggest deposition under euxinic conditions (Fe_{HR}/Fe_T >0.38 and Fe_{py}/Fe_{HR} >0.60), only six yield Mo_{EF} >1 and none yield both Mo_{EF} and U_{EF} >1 (Fig. 2I). The upper part of Member I, and Members II and III, were likely deposited under oxic bottom water conditions, as evidenced by persistently low Fe_{HR}/Fe_T ratios, along with no indication of anoxic or suboxic conditions from enrichments in Mo or U (Fig. 2, Tribovillard et al., 2012). As such, these intervals are unlikely to record the Mo isotopic composition of seawater.

Elevated Fe_{HR}/Fe_T ratios (>0.38) occur throughout the Xiangtan section (Fig. 3), while Fe_{py}/Fe_{HR} ratios fluctuate considerably (0.49–0.88). In total, 12 samples have Fe_{py}/Fe_{HR} ratios >0.6, indicating possible euxinic depositional conditions. However, the extent of Mo and U enrichment varies (Fig. 3), with only three samples exhibiting Mo_{EF} >1 and only one sample with both Mo_{EF} and U_{EF} >1, which

312 independently support euxinic water column conditions (Fig. 3H). This suggests that the majority of
313 elevated Fe_{py}/Fe_{HR} values may instead result primarily from the development of sulfidic porewaters.
314
315 *5.3 Formation of Mn-carbonate and its influence on Mo concentrations and isotopes in adjacent black*
316 *shales*
317 The widespread Mn-carbonate unit in the basal Datangpo Formation is interpreted to have formed
318 through a two-stage process: (1) primary deposition of Mn oxides in an oxic water column, followed by
319 (2) diagenetic transformation to Mn-carbonate (Wang et al., 2025). During the second stage, reductive
320 dissolution of the Mn oxides, coupled with organic matter oxidation during early diagenesis, released
321 Mn^{2+} and CO_3^{2-} that ultimately precipitated as Mn-carbonate ($MnCO_3$). Laboratory adsorption
322 experiments have established that manganese (oxyhydr)oxides (MnOx) exhibit a strong affinity for Mo
323 (Barling et al., 2004). The deposition of Mn oxides (MnO_x) would have preferentially sequestered lighter
324 Mo isotopes, resulting in isotopically heavy Mo-enriched residual seawater, with a characteristic
325 fractionation factor ($\Delta^{98}Mo_{ocean\text{-}MnOx}$ = 3‰, Barling et al., 2004). Subsequent diagenetic reduction would
326 have released this fractionated Mo into porewaters, and there may have been multiple cycles of
327 adsorption and release. Therefore, unlike pristine, non-skeletal carbonates, manganese carbonates are
328 highly unlikely to record the Mo isotopic composition of Cryogenian seawater.
329 The patterns of Mo distribution provide additional evidence for this transformation process. In the
330 Daotuo section, Mn-carbonate layers have much lower Mo concentrations (commonly <1 μg/g)
331 compared to adjacent euxinic black shales (commonly >10 μg/g). The majority of shale samples from
332 the lower part of the Daotuo section also contain significantly greater Mo relative to samples from the
333 lower Xiangtan section (max. 3.79 μg/g). We propose that the observed geochemical patterns result from
334 diagenetic Mo remobilization during Mn-carbonate formation: (1) initially, reductive dissolution of Mn-
335 oxide precursors released adsorbed Mo into porewaters; (2) subsequently, the liberated Mo was captured
336 by organic matter and pyrite in the sulfidic porewaters of adjacent black shales (Scholz et al., 2018). This
337 process explains both the exceptionally low Mo concentrations (<1 μg/g) in Mn-carbonates and the
338 elevated Mo levels (>10 μg/g) in neighboring euxinic shales, and is also consistent with the
339 transformation of Mn-oxides to carbonates following the Sturtian deglaciation. By contrast, the low
340 average Mo concentrations in the Xiangtan section shales reflect the absence of such Mn-carbonate layers
341 and associated diagenetic Mo release.

In the Daotuo section, most samples from the upper part of Member I, and Members II and III, yield Fe_{HR}/Fe_T <0.38, and hence would not capture the $\delta^{98}Mo$ composition of seawater, with $\delta^{98}Mo$ values that are lower than or equal to that of the bulk silicate Earth. The $\delta^{98}Mo$ compositions of samples from Member I vary dramatically. Twelve samples have Fe_{py}/Fe_{HR} ratios >0.60 and yield $\delta^{98}Mo$ values in the range -0.08 to 1.31‰. However, as noted above, not all of these samples are interpreted to have been deposited under euxinic water column conditions, based on the absence of Mo or U enrichment. Six anoxic samples filtered for Fe_{py}/Fe_{HR} >0.60 and Mo_{EF} >1 yield $\delta^{98}Mo$ in the range -0.08 to 0.80‰ (Fig. 2I). The heaviest value obtained from these potentially euxinic samples (0.80 ± 0.11‰) is considered to represent the best approximation of the $\delta^{98}Mo$ composition of early non-Snowball seawater (e.g., Neubert et al. 2008; Dahl et al. 2010; Nägler et al. 2011).

The $\delta^{98}Mo$ values in euxinic black shales adjacent to Mn-carbonate layers in the lower Datangpo Formation (documented in the Minle, Xixibao, Changxingpo and Daotuo sections) likely reflect local diagenetic processes rather than contemporaneous seawater composition. This is because: (1) Mn oxides preferentially adsorb lighter Mo during deposition, (2) subsequent diagenetic reduction releases this fractionated Mo into porewaters, and (3) re-precipitation in sulfidic environments further alters the Mo isotopic signature of contemporaneous seawater. Consequently, while these values provide important insight into local redox dynamics, they cannot be reliably used as proxies for global seawater $\delta^{98}Mo$ during this interval. The observed signatures instead represent the integrated product of depositional and post-depositional processes characteristic of Mn-rich sedimentary systems, and as such we do not use these values to model the spatial extent of different redox conditions in the global ocean (see below). This multiphase history necessitates careful recalibration of published Mo isotope data (e.g., Chen et al., 2015; Pan et al., 2021; Tan et al., 2021) from the lower part of Member I in the Datangpo Formation.

The stratigraphic alternation between Mn-rich layers and organic-rich black shales in lower Member I from the Daotuo section records dynamic redox fluctuations during Cryogenian deposition. Mn oxide precipitation occurred in oxic water masses, while black shale deposition likely occurred under euxinic conditions (Section 5.2). This rhythmic sedimentary sequence indicates that the chemocline between oxic/anoxic and euxinic water masses was mobile, with the Daotuo section positioned near this fluctuating redox boundary (Li et al., 2012). These observations demonstrate that while elevated Mn^{2+} concentrations in Cryogenian seawater were a prerequisite for Mn mineralization, the ultimate deposition of Mn (oxyhydr)oxides was fundamentally controlled by redox conditions at the depositional site. Thus,

the Mn-rich layers mark specific time intervals when oxygenated waters expanded sufficiently to allow precipitation of Mn oxides before the return of euxinic conditions.

5.4 Changing [Mo] reservoir size in the Cryogenian non-Snowball ocean

As noted above, calculated enrichment factors for redox sensitive trace elements represent enrichment (X_{EF}>1) or depletion (X_{EF}<1) relative to the average upper continental crust (UCC compositions after McLennan, 2001). The fact that non-Snowball sedimentary rocks from the Nanhua Basin yield enrichment factors <1 illustrates that the background supply of detrital U and Mo to the Nanhua Basin was unusually low relative to the UCC (Fig. 4A). It is also clear that modern open marine environments, which are used to define specific drawdown mechanisms for Mo and U enrichment, are not appropriate for the definition of post-Sturtian depositional redox conditions. In particular, the concentrations of Mo and U in the Nanhua Basin water column immediately following the Sturtian deglaciation were likely lower than they are today, particularly due to the long-term (60 Myr) drawdown of trace metals that occurred under predominately anoxic Snowball ocean conditions and the low rate of resupply from relatively low oxidative weathering (Siebert et al., 2003; Asael et al., 2018; Scheller et al., 2018; Bowyer et al., 2023).

Molybdenum enrichment factors are commonly elevated in samples where Fe speciation data indicate anoxic deposition (Fig. 4B, see also Bowyer et al., 2023). This is consistent with the idea that Mo drawdown was controlled by sulfide availability rather than by an Fe-Mn (oxyhydr)oxide particulate shuttle (Fe-Mn shuttle).

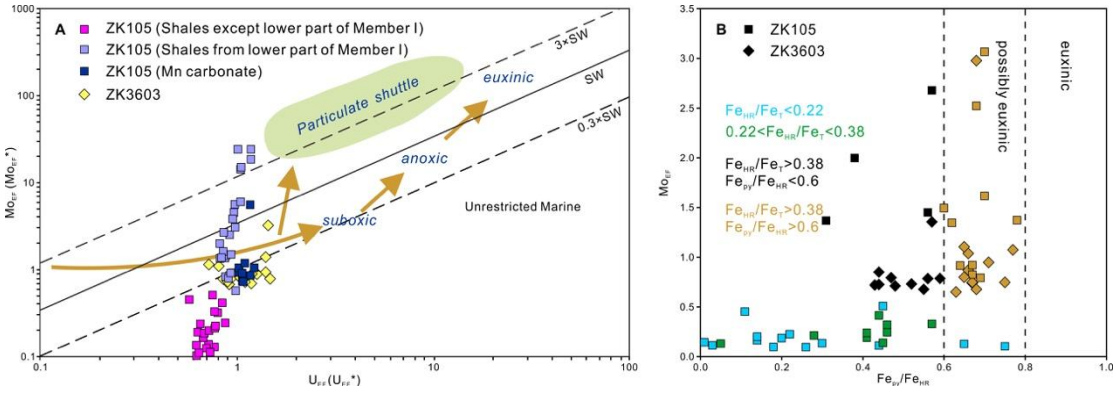

Fig. 4. Mo_{EF} vs. U_{EF} (A) and Mo_{EF} vs. Fe_{py}/Fe_{HR} (B) for analyzed Cryogenian shales of ZK105 (Zhang et al., 2015) and ZK3603 (Bowyer et al., 2023). Solid lines and dashed lines in (A) represent multiples of the Mo/U molar ratio of modern seawater (×0.3, ×1, and ×3). Different redox and particulate shuttle

fields are modified from Algeo and Tribovillard (2009). The "particulate shuttle" is linked to Fe-Mn redox cycling within the water column. Note that Mo_{EF} scales with the degree of sulfidization of the Fe_{HR} pool (B), which suggests that the primary control on Mo drawdown was sulfide availability, rather than an Fe-Mn shuttle.

Globally distributed Cryogenian non-Snowball strata yield uniformly low Mo concentrations (<50 μg/g), as documented in the Datangpo Formation (South China), the MacDonaldryggen Member of the Elbobreen Formation (Svalbard), the Arena Formation (east Greenland), and the Twitya Formation (northwest Canada) (Li et al., 2012, Ye et al., 2018; Ma et al., 2019; Kunzmann et al., 2015; Sperling et al., 2015; Scheller et al., 2018; Pan et al., 2021; Tan et al., 2021). Several of the interpreted depositional environments are thought to have been at least intermittently connected to the global ocean, especially in the immediate post-Sturtian aftermath, supporting the notion that the Cryogenian non-Snowball interval was characterized by a depleted oceanic Mo reservoir (Scheller et al., 2018; Pan et al., 2021).

To constrain seawater Mo concentrations during the Cryogenian, we collate the Mo concentrations of globally distributed euxinic shales at this time (Bowyer et al., 2023; Zhang et al., 2015; Shi et al., 2016) following established methodologies (Scott et al., 2008; Luo et al., 2021). We use a recent time-calibrated compilation of published global data (Fig. 5A, Bowyer et al., 2023) and screen each individual dataset using the same criteria as our newly published data to distinguish the samples most likely to have been deposited under euxinic conditions (Table S3). Given the issues outlined above regarding the likelihood of Mo redistribution during Mn-carbonate formation, we avoid shale samples that are interbedded with, or in close proximity to, extensive Mn-carbonate deposits.

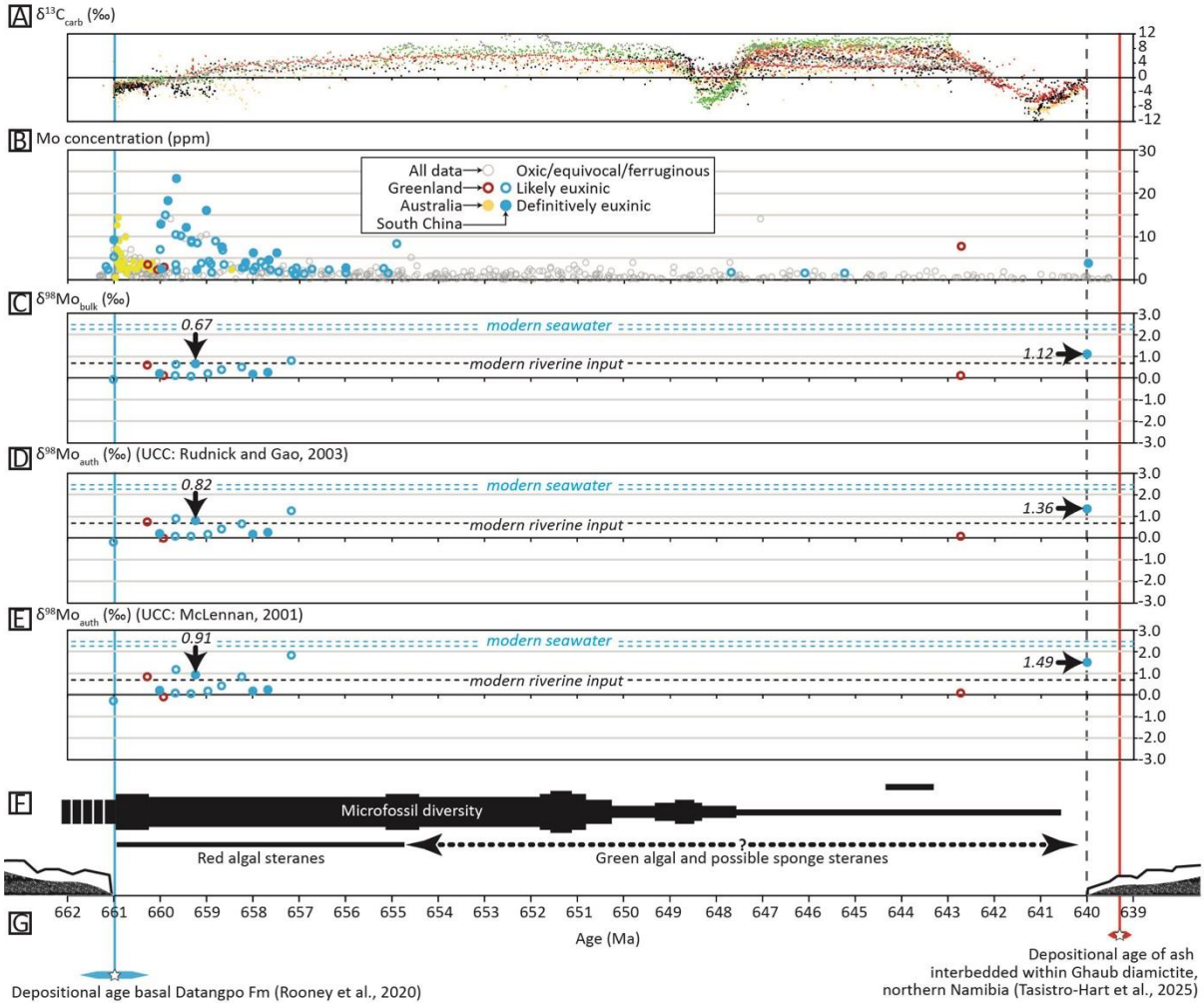

Fig. 5. Global compilation of data from the Cryogenian non-Snowball interval, including (A) $\delta^{13}C_{carb}$, (B) [Mo] (screening criteria – likely euxinic: Fe_{HR}/Fe_T >0.38, Fe_{py}/Fe_{HR} >0.60, Mo_{EF} >1; definitively euxinic: Fe_{HR}/Fe_T >0.38, Fe_{py}/Fe_{HR} >0.60, Mo_{EF} >1, U_{EF} >1), (C-E) δ^{98}Mo data from Scheller et al. (2018), Pan et al. (2021) and this study. Authigenic δ^{98}Mo data in panels (D) and (E) were calculated using UCC compositions of Rudnick and Gao (2003) and McLennan (2001), respectively. (F) temporally calibrated biotic summary. (G) radioisotopic ages that constrain the maximum age of Sturtian deglaciation (Rooney et al., 2020) and the minimum age of Marinoan onset (Prave et al., 2016; Tasistro-Hart et al., 2025). Arrowed datapoints in (C-E) correspond to two δ^{98}Mo samples that are used in the modelling, which can be confidently interpreted as having been deposited under euxinic bottom water conditions. These define an increase in seawater δ^{98}Mo from the earlier part of the non-Snowball interval to the later part of the non-Snowball interval. Compilation and age calibration of carbon, molybdenum and fossil data after Model D of Bowyer et al. (2023), assuming a short-duration Marinoan Snowball consistent with the interpretations of Tasistro-Hart et al. (2025).

Assuming near-quantitative Mo drawdown under sulfidic conditions (H_2S_{aq} >11 μmol/L), our approach yields an early non-Snowball interval where maximum sediment Mo concentrations reached 23.36 μg/g in the Nanhua Basin (Fig. 5B, Cheng et al., 2018), which is greater than the Mo concentrations of definitively euxinic sediments from Australia (max. = 14.39 ug/g, Bowyer et al., 2023) and likely euxinic sediments of the Arena Formation of east Greenland (max. = 7.8 ug/g, Scheller et al., 2018). This early stage of elevated [Mo] broadly coincides with a globally-recognized euxinic episode in the immediate Sturtian aftermath (e.g., Bowyer et al., 2023 and references therein). A decrease in the [Mo] of euxinic sedimentary rocks following this interval is consistent with depletion of the seawater Mo reservoir as a consequence of globally expanded anoxia (Scheller et al., 2018; Bowyer et al., 2023). It may also reflect a gradual decrease in the weathering input of Mo following the early post-Sturtian super-greenhouse weathering pulse (e.g., Brocks et al., 2017; Bowyer et al., 2023). Samples deposited under euxinic conditions become extremely rare thereafter, and are only recovered in the Arena Formation of Greenland and the Xiangmeng Formation of the Nanhua Basin (Fig. 5B). A possibly euxinic sample from the Arena Formation yields [Mo] as high as 7.80 ug/g (Scheller et al., 2018), which may attest to an intermediate sized Mo reservoir in the latter half of the non-Snowball interval, but [Mo] is as low as 3.79 ug/g in a definitively euxinic sample from the upper Xiangmeng Formation at Xiangtan section (Fig. 5B). Together, these data support a long-term decrease in the size of the seawater Mo reservoir throughout the non-Snowball interval.

5.5. Constraining global marine redox evolution of the mid-Cryogenian non-Snowball ocean

The maximum δ^{98}Mo value from euxinic, organic-rich mudrocks for any time interval provides the most conservative estimate of the seawater δ^{98}Mo composition (Kendall et al., 2017), assuming that Mo isotope fractionation during Mo–sulfide precipitation is ca. 0.9‰ relative to contemporaneous seawater (Poulson Brucker et al., 2012). In addition to the Nanhua Basin, δ^{98}Mo data from the Arena Formation (ranging from -0.86 to 1.47‰) have also been interpreted to represent widespread marine anoxia (Scheller et al., 2018). However, some data from the Arena Formation, especially those near the top of the studied section, are difficult to interpret due to complications in extrapolating global seawater δ^{98}Mo using values that may have fractionated during non-quantitative Mo drawdown under non-euxinic water column conditions (Scheller et al., 2018). Potential problems related to depositional duration and non-quantitative Mo drawdown may be resolvable when considering the data presented here from euxinic

462 samples of the continuous Xiangtan section, relative to the Arena Formation record (Fig. 5).

463 As noted above, three samples from the upper part of the Xiangtan section that yield Fe_{HR}/Fe_T >0.38,
464 Fe_{py}/Fe_{HR} >0.6 and Mo_{EF} >1 are the most likely to capture euxinic depositional conditions at Xiangtan
465 (Fig. 3). The stratigraphically highest of these samples also yields U_{EF} >1 and a $\delta^{98}Mo$ value of +1.12 ±
466 0.09‰, which we consider to represent the most conservative estimate of seawater $\delta^{98}Mo$.

467 After careful consideration of regional depositional redox conditions, alongside previously
468 published data, samples that robustly capture seawater $\delta^{98}Mo$ show a long-term shift in bulk $\delta^{98}Mo$ from
469 +0.67 ± 0.06‰ in the earlier part of the Cryogenian non-Snowball interval (data from the Xixibao core
470 of the Nanhua Basin, reported by Pan et al., 2021) to +1.12 ± 0.09‰ toward the end of the interval (data
471 from Xiangtan core, reported herein, Fig 5C). We note, however, that these data are temporally patchy
472 and do not preclude the possibility for intervening intervals of global redox variability that remain
473 obscured by a paucity of samples that were deposited under definitively euxinic conditions.

474 Pan et al. (2021) also emphasized the need to correct for the influence of the detrital Mo fraction on
475 $\delta^{98}Mo$ data, especially since many bulk $\delta^{98}Mo$ values are only slightly higher than the UCC value of
476 +0.3‰ (Voegelin et al., 2014). As such, we follow the criteria of Pan et al. (2021) by discounting data
477 with Mo_{EF} <2 from further discussion, based on recognition that these samples still contain a large
478 proportion of detrital Mo. Authigenic $\delta^{98}Mo$ values were then calculated after Tribovillard et al. (2006)
479 and Kendall et al. (2015), as follows:

480 $$\delta^{98}Mo_{auth} = \delta^{98}Mo_{bulk} - (Al/Mo)_{bulk} * \{(\delta^{98}Mo_{det} - \delta^{98}Mo_{bulk})/[(Al/Mo)_{det} - (Al/Mo)_{bulk}]\}$$

481 where "auth" = authigenic, "bulk" = bulk or total sample, and "det" = detrital. The composition of detrital
482 fractions were assumed to approximate UCC compositions, and $\delta^{98}Mo_{auth}$ values were calculated using
483 UCC compositions from both McLennan (2001) and Rudnick and Gao (2003), for comparison (Fig. 5D,
484 E). The most elevated $\delta^{98}Mo_{auth}$ values arose when using the UCC compositions of McLennan (2001)
485 (Fig. 5E, Table S3).

486 To constrain the global redox state of the ocean during deposition of Cryogenian non-Snowball
487 sediments, we use a single reservoir Mo cycling model with a fixed riverine input composition and three
488 sinks for oxic, reducing non-euxinic (i.e., ferruginous) and euxinic conditions, based on the model of
489 Luo et al. (2021). The initial model conditions, flux, and reservoir calculations are the same as those in
490 Luo et al. (2021) (Table S5). The model was run multiple times for randomly chosen areas of oxic,
491 euxinic and ferruginous seafloor, and outputs were retained when they satisfy shifts in the oceanic Mo

concentration from 23.4 ug/g (early non-Snowball) to 3.8 ug/g (late non-Snowball), and seawater $\delta^{98}Mo$ values based on measured $\delta^{98}Mo_{bulk}$ compositions of +0.67 to +0.91‰ (maximum bulk and authigenic values for the early non-Snowball) and +1.12 to +1.49‰ (maximum bulk and authigenic values for the late non-Snowball). We also impose a 10x reduction in weathering input from the early to late non-Snowball, which replicates the expected order of magnitude decrease in weathering driven by the shift from a post-Sturtian super-greenhouse climate with abundant deglacial input to a milder climate lacking additional input. The results of 200,000 model runs are plotted in Fig. 6, with overlaps in the red shaded areas defining where both the Mo concentrations and Mo isotopic values are satisfied.

Our quantitative modeling allows us to estimate the most probable seafloor redox architecture during the Cryogenian non-Snowball interval. Both solutions indicate the presence of a large area of anoxic seafloor (potentially around 20%) throughout the mid-Cryogenian interval. The model results also support the possibility of a higher euxinic seafloor area in the early non-Snowball, which is observable in the regional redox record and is required to drive the smaller fractionation in $\delta^{98}Mo$ in the model through a greater proportion of non-fractionating Mo sinks. The reduced Mo concentration in the later period requires larger sinks overall in the model, but these roughly balance the assumed reduction in the input flux from weathering.

The predicted reduction in euxinic areas from the early to late non-Snowball interval, in addition to evidence for a brief global-scale oxygenation event during the Sturtian deglaciation (which is also permissible in the model in panel A), may have a causal relationship with biotic evolution. A temporal calibration of biotic information for the non-Snowball interval is presented alongside our updated Mo record in Fig. 5F (chemostratigraphic age model after Bowyer et al., 2023). This shows that the maximum possible age of biomarker data that track both the rise to dominance of green algal primary production and the earliest putative evidence for animal life post-dates the decrease in the areal extent of euxinic conditions.

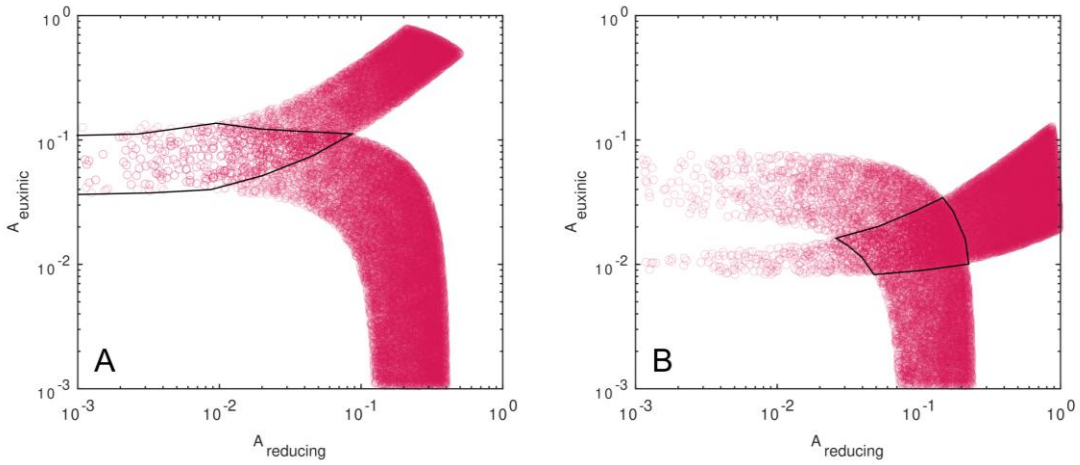

Fig. 6. Model output results of the isotope mass balance satisfying (A) early non-Snowball [Mo] = 23.4 μg/g and $\delta^{98}Mo_{bulk}$ = +0.67 ± 0.06‰ and (B) late non-Snowball [Mo] = 3.8 ug/g and $\delta^{98}Mo$ = +1.12 ± 0.09‰. For each panel, the two red zones show the models that satisfy either the isotope value or concentration constraints, and the intersection shown with a black outline indicates the regions that satisfy both constraints.

6. Conclusions

1. Basin-wide deposition of Mn-rich carbonates immediately following the Sturtian deglaciation was associated with significant $\delta^{98}Mo$ fractionation, which obscures primary seawater $\delta^{98}Mo$ compositions in the basal Datangpo Formation. This multiphase history necessitates careful reconsideration of the utility of Mo isotope data from lower Member I of the Datangpo Formation to inform seawater composition.

2. The lower part of Member I of the Daotuo section (Datangpo Formation) records deposition under oscillatory redox conditions. Mn oxide precipitation occurred under oxic water column conditions, while black shale deposition likely occurred under dominantly euxinic conditions. This indicates that the chemocline separating oxic/anoxic and euxinic water masses was mobile, and the Daotuo section was positioned near this fluctuating redox boundary.

3. Based on careful consideration of global multi-proxy data, this study establishes a shift from a larger early non-Snowball seawater Mo reservoir that resulted in maximum values of 23.4 μg/g Mo in euxinic sediments, followed by a decrease in the size of the seawater Mo reservoir that resulted in late non-Snowball euxinic sediments with Mo concentrations of 3.8 ug/g. This shift may result from global changes in both weathering input and oceanic redox during the mid-Cryogenian.

4. The Xiangtan section serves as a valuable, possibly unique, archive to reconstruct seawater δ^{98}Mo throughout the Cryogenian non-Snowball interval, as it represents one of the only sections known that records continuous deposition within the anoxic deeper part of the water column. Available data from samples that were deposited under definitively euxinic depositional conditions in Xixibao and Xiangtan sections constrain a shift in bulk δ^{98}Mo from +0.67 ± 0.06‰ in the early non-Snowball interval to +1.12 ± 0.09‰ in the late non-Snowball interval.

5. Our single reservoir Mo cycling model suggests that the global seafloor was characterized by substantial anoxia throughout the non-Snowball interlude. It also suggests that euxinic conditions were more globally widespread in the aftermath of Sturtian Snowball deglaciation, and may have declined in advance of the Marinoan Snowball, broadly coincident with the maximum age of biomarker evidence for the emergence of animals and the rise of green algae. However, this record remains sparse due to the paucity of definitively euxinic deposits, and the possibility therefore remains for higher-order global redox variability throughout the non-Snowball interval.

7. Acknowledgements

This study was financially supported by the National Key R&D Program of China (2022YFF0800104), the Joint Program of National Natural Science Foundation of China (U2244210) and the National Natural Science Foundation of China (41973020). FTB and SWP acknowledge funding from NERC project NE/R010129/1. Author contributions: JL and XZ conceived the project. XP and BY assisted with sample collection. JL analysed samples for δ^{98}Mo, and JL and FTB analyzed samples for Fe speciation. JL and XZ interpreted the data. BJWM developed the biogeochemical model. JL wrote the first draft of the paper and all authors contributed to the final paper.

References

Alcott, L.J., Krause, A.J., Hammarlund, E.U., Bjerrum, C.J., Scholz, F., Xiong, Y., Hobson, A.J., Neve, L., Mills, B.J.W., März, C., Schnetger, B., Bekker, A., Poulton, S.W., 2020. Development of Iron Speciation Reference Materials for Palaeoredox Analysis. Geostand. Geoanal. Res. 44, 581–591. https://doi.org/10.1111/ggr.12342

Algeo, T.J., Tribovillard, N., 2009. Environmental analysis of paleoceanographic systems based on molybdenum–uranium covariation. Chem. Geol. 268, 211–225. https://doi.org/10.1016/j.chemgeo.2009.09.001

Allen, P.A., Leather, J., Brasier, M.D., Rieu, R., McCarron, M., Le Guerroué, E., Etienne, J.L., Cozzi, A., 2011. The Abu Mahara Group (Ghubrah and Fiq formations), Jabal Akhdar, Oman. Chapter 20 in Arnaud, E., Halverson, G.P., Shields-Zhou, G. (eds) The Geological Record of Neoproterozoic Glaciations. Geological Society, London, Memoirs 36, 251–262. https://doi.org/10.1144/M36

Arnold, G.L., Anbar, A.D., Barling, J., Lyons, T.W., 2004. Molybdenum isotope evidence for widespread anoxia in mid-Proterozoic oceans. Science 304, 87–90. https://doi.org/10.1126/science.1091785

Asael, D., Rouxel, O., Poulton, S., Lyons, T., Bekker, A., 2018. Molybdenum record from black shales indicates oscillating atmospheric oxygen levels in the early Paleoproterozoic. Am. J. Sci. 318, 275–299. https://doi.org/10.2475/03.2018.01

Bao, X., Zhang, S., Jiang, G., Wu, H., Li, H., Wang, X., An, Z., Yang, T., 2018. Cyclostratigraphic constraints on the duration of the Datangpo Formation and the onset age of the Nantuo (Marinoan) glaciation in South China. Earth Planet. Sci. Lett. 483, 52–63. https://doi.org/10.1016/j.epsl.2017.12.001

Barling, J., Anbar, A.D., 2004. Molybdenum isotope fractionation during adsorption by manganese oxides. Earth Planet. Sci. Lett. 217, 315–329. https://doi.org/10.1016/S0012-821X(03)00608-3

Benkovitz, A., Matthews, A., Teutsch, N., Poulton, S.W., Bar-Matthews, M., Almogi-Labin, A., 2020. Tracing water column euxinia in Eastern Mediterranean Sapropels S5 and S7. Chem. Geol. 545, 119627. https://doi.org/10.1016/j.chemgeo.2020.119627

Bowyer, F.T., Krause, A.J., Song, Y., Huang, K.-J., Fu, Y., Shen, B., Li, J., Zhu, X.-K., Kipp, M.A., van Maldegem, L.M., Brocks, J.J., Shields, G.A., Le Hir, G., Mills, B.J.W., Poulton, S.W., 2023. Biological diversification linked to environmental stabilization following the Sturtian Snowball

593 glaciation. Sci. Adv. 9, eadf9999. https://doi.org/10.1126/sciadv.adf9999
594 Brocks, J.J., Jarrett, A.J.M., Sirantoine, E., Hallmann, C., Hoshino, Y., Liyanage, T., 2017. The rise of
595 algae in Cryogenian oceans and the emergence of animals. Nature 548, 578–581.
596 https://doi.org/10.1038/nature23457
597 Brocks, J.J., Nettersheim, B.J., Adam, P., Schaeffer, P., Jarrett, A.J.M., Güneli, N., Liyanage, T., vasn
598 Maldegem, L.M., Hallmann, C., Hope, J.M., 2023. Lost world of complex life and the late rise of
599 the eukaryotic crown. Nature 618(7966), 767–773. http://doi.org/10.1038/s41586-06170-w.
600 Canfield, D., Raiswell, R., Westrich, J.T., Reaves, C.M., Berner, R.A., 1986. The use of chromium
601 reduction in the analysis of reduced inorganic sulfur in sediments and shales. Chem. Geol. 54,
602 149–155. https://doi.org/10.1016/0009-2541(86)90078-1
603 Canfield, D.E., Poulton, S.W., Knoll, A.H., Narbonne, G.M., Ross, G., Goldberg, T., Strauss, H., 2008.
604 Ferruginous conditions dominated later neoproterozoic deep-water chemistry. Science 321, 949–
605 952. https://doi.org/10.1126/science.1154499
606 Chen, X., Ling, H.F., Vance, D., Shields-Zhou, G.A., Zhu, M., Poulton, S.W., Och, L.M., Jiang, S.Y.,
607 Li, D., Cremonese, L., Archer, C., 2015. Rise to modern levels of ocean oxygenation coincided
608 with the Cambrian radiation of animals. Nat. Commun. 6, 7. https://doi.org/10.1038/ncomms8142
609 Cheng, M., Li, C., Chen, X., Zhou, L., Algeo, T., Ling, H.-F., Feng, L.-J., Jin, C.-S., 2018. Delayed
610 Neoproterozoic oceanic oxygenation: Evidence from Mo isotopes of the Cryogenian Datangpo
611 Formation. Precambrian Res. 319, 187–197. https://doi.org/10.1016/j.precamres.2017.12.007
612 Cheng, M., Zhang, Z., Algeo, T.J., Liu, S., Liu, X., Wang, H., Chang, B., Jin, C., Pan, W., Cao, M., Li,
613 C., 2021. Hydrological controls on marine chemistry in the Cryogenian Nanhua Basin (South
614 China). Earth-Science Reviews 218, 103678. https://doi.org/10.1016/j.earscirev.2021.103678
615 Condon, D., Zhu, M., Bowring, S., Wang, W., Yang, A., Jin, Y., 2005. U-Pb ages from the
616 Neoproterozoic Doushantuo Formation, China. Science 308, 95–98.
617 https://doi.org/10.1126/science.1107765
618 Dahl, T.W., Anbar, A.D., Gordon, G.W., Rosing, M.T., Frei, R., Canfield, D.E., 2010. The behavior of
619 molybdenum and its isotopes across the chemocline and in the sediments of sulfidic Lake
620 Cadagno, Switzerland. Geochim. Cosmochim. Acta 74, 144–163.
621 https://doi.org/10.1016/j.gca.2009.09.018
622 Dahl, T.W., Canfield, D.E., Rosing, M.T., Frei, R.E., Gordon, G.W., Knoll, A.H., Anbar, A.D., 2011.

623 Molybdenum evidence for expansive sulfidic water masses in 750 Ma oceans. Earth Planet. Sci.
624 Lett. 311, 264–274. https://doi.org/10.1016/j.epsl.2011.09.016
625 Du, Y.S., Zhou, Q., Yu, W.C., Wang, P., Yuan, L., Qi, L., Guo, H., Xu, Y., 2015. Linking the Cryogenian
626 manganese metallogenic process in the southeast margin of Yangtze Block to breakup of Rodinia
627 supercontinent and Sturtian Glaciation. Geol. Sci. Technol. Inf. 34, 1–7 (In Chinese with English
628 abstract).
629 Gaspers, N., Magna, T., Ackerman, L., 2020. Molybdenum Mass Fractions and Stable Isotope
630 Compositions of Sedimentary Carbonate and Silicate Reference Materials. Geostandards and
631 Geoanalytical Research 44(2), 363–374. https://doi.org/10.1111/ggr.12314
632 Goldberg, T., Archer, C., Vance, D., Poulton, S.W., 2009. Mo isotope fractionation during adsorption to
633 Fe (oxyhydr)oxides. Geochim. Cosmochim. Acta 73, 6502–6516.
634 https://doi.org/10.1016/j.gca.2009.08.004
635 Goldberg, T., Archer, C., Vance, D., Thamdrup, B., McAnena, A., Poulton, S.W., 2012. Controls on Mo
636 isotope fractionations in a Mn-rich anoxic marine sediment, Gullmar Fjord, Sweden. Chem. Geol.
637 296–297, 73–82. https://doi.org/10.1016/j.chemgeo.2011.12.020
638 Helz, G.R., Miller, C.V., Charnock, J., Mosselmans, J.F., Pattrick, R., Garner, C., Vaughan, D.J., 1996.
639 Mechanism of molybdenum removal from the sea and its concentration in black shales: EXAFS
640 evidence. Geochim. Cosmochim. Acta 60, 3631–3642. https://doi.org/10.1016/0016-
641 7037(96)00195-0
642 Hoffman, P., Abbot, D., Ashkenazy, Y., Benn, D., Brocks, J., Cohen, P., Cox, G., Creveling, J.,
643 Donnadieu, Y., Erwin, D., Fairchild, I., Ferreira, D., Goodman, J., Halverson, G., Jansen, M., Hir,
644 G., Love, G., Macdonald, F., Maloof, A., Warren, S., 2017. Snowball Earth climate dynamics and
645 Cryogenian geology-geobiology. Sci. Adv. 3, e1600983. https://doi.org/10.1126/sciadv.1600983
646 Hoffman, P.F., Kaufman, A.J., Halverson, G.P., Schrag, D.P., 1998. A Neoproterozoic Snowball Earth.
647 Science 281, 1342–1346. https://doi.org/10.1126/science.281.5381.1342
648 Kendall, B., Dahl, T.W., Anbar, A.D., 2017. The stable isotope geochemistry of Molybdenum. Reviews
649 in Mineralogy and Geochemistry 82, 683–732. https://doi.org/10.2138/rmg.2017.82.16
650 Krewer, C., Poulton, S. W., Newton, R. J., März, C., Mills, B. J. W., Wagner, T., 2024. Controls on the
651 Termination of Cretaceous Oceanic Anoxic Event 2 in the Tarfaya Basin, Morocco. American
652 Journal of Science 324, 11. https://doi.org/10.2475/001c.118797

653 Kunzmann, M., Halverson, G.P., Scott, C., Minarik, W.G., Wing, B.A., 2015. Geochemistry of
654 Neoproterozoic black shales from Svalbard: Implications for oceanic redox conditions spanning
655 Cryogenian glaciations. Chem. Geol. 417, 383–393.
656 http://dx.doi.org/10.1016/j.chemgeo.2015.10.022
657 Lan, Z., Li, X., Zhu, M., Chen, Z.-Q., Zhang, Q., Li, Q., Lu, D., Liu, Y., Tang, G., 2014. A rapid and
658 synchronous initiation of the widespread Cryogenian glaciations. Precambrian Res. 255, 401–411.
659 https://doi.org/10.1016/j.precamres.2014.10.015
660 Lau, K.V., Macdonald, F.A., Maher, K., Payne, J.L., 2017. Uranium isotope evidence for temporary
661 ocean oxygenation in the aftermath of the Sturtian Snowball Earth. Earth Planet. Sci. Lett. 458,
662 282–292. https://doi.org/10.1016/j.epsl.2016.10.043
663 Li, C., Love, G.D., Lyons, T.W., Scott, C.T., Feng, L., Huang, J., Chang, H., Zhang, Q., Chu, X., 2012.
664 Evidence for a redox stratified Cryogenian marine basin, Datangpo Formation, South China. Earth
665 Planet. Sci. Lett. 331–332, 246–256. https://doi.org/10.1016/j.epsl.2012.03.018
666 Li, J., Zhu, X.-k., Tang, S.-h., Zhang, K., 2016. High-Precision Measurement of Molybdenum Isotopic
667 Compositions of Selected Geochemical Reference Materials. Geostand. Geoanal. Res. 40, 405–
668 415. https://doi.org/10.1111/j.1751-908X.2015.00369.x
669 Li, J., Zhu, X.K., Tang, S.H., 2022. Assessment of Different Digestion Procedures for Mo Isotope
670 Measurements of Black and Grey Shales Using the Double Spike Technique. Journal of Earth
671 Science 33(1), 76–81. https://doi.org/10.1007/s12583-021-1520-1.
672 Love, G.D., Grosjean, E., Stalvies, C., Fike, D.A., Grotzinger, J.P., Bradley, A.S., Kelly, A.E., Bhatia,
673 M., Meredith, W., Snape, C.E., Bowring, S.A., Condon, D.J., Summons, R.E., 2009. Fossil
674 steroids record the appearance of Demospongiae during the Cryogenian period. Nature 457, 718–
675 722. http://doi.org/10.1038/nature07673.
676 Luo, J., Long, X., Bowyer, F.T., Mills, B., Poulton, S.W., 2021. Pulsed oxygenation events drove
677 progressive oxygenation of the early Mesoproterozoic ocean. Earth Planet. Sci. Lett. 559, 116754.
678 https://doi.org/10.1016/j.epsl.2021.116754
679 Ma, X.C., Wang, J.S., Algeo, T.J., Wang, Z., Cen, Y., Chen, C., Chen, D.H., Lu, J.C., Yang, Y.Z., 2023.
680 U-Pb dating of detrital zircons from the Datangpo Formation, South China: Implications for
681 Sturtian deglaciation age and Nanhua stratal provenance. Palaeogeogr. Palaeoclimatol. Palaeoecol.
682 617, 111494. https://doi.org/10.1016/j.palaeo.2023.111494

683 Ma, Z.X., Liu, X.T., Yu, W.C., Du, Y.S., Du, Q.D., 2019. Redox conditions and manganese
684 metallogenesis in the Cryogenian Nanhua Basin: insight from the basal Datangpo Formation of
685 South China. Palaeogeogr. Palaeoclimatol. Palaeoecol. 529, 39–52.
686 https://doi.org/10.1016/j.palaeo.2019.05.031
687 McLennan, S.M., 2001. Relationships between the trace element composition of sedimentary rocks and
688 upper continental crust. Geochem. Geophys. Geosyst. 2, 2000GC000109.
689 https://doi.org/10.1029/2000GC000109
690 Miller, C.A., Peucker-Ehrenbrink, B., Walker, B.D., Marcantonio, F., 2011. Re-assessing the surface
691 cycling of molybdenum and rhenium. Geochim. Cosmochim. Acta 75, 7146–7179.
692 https://doi.org/10.1016/j.gca.2011.09.005
693 Nägler, T.F., Siebert, C., Luschen, H., Bottcher, M.E., 2005. Sedimentary Mo isotope record across the
694 Holocene fresh–brackish water transition of the Black Sea. Chem. Geol. 219, 283–295.
695 https://doi.org/10.1016/j.chemgeo.2005.03.006
696 Nägler, T.F., Neubert, N., Böttcher, M.E., Dellwig, O., Schnetger, B., 2011. Molybdenum isotope
697 fractionation in pelagic euxinia: evidence from the modern Black and Baltic Seas. Chem. Geol.
698 289, 1–11. https://doi.org/10.1016/j.chemgeo.2011.07.001
699 Nägler, T.F., Anbar, A.D., Archer, C., Goldberg, T., Gordon, G.W., Greber, N.D., Siebert, C., Sohrin, Y.,
700 Vance, D., 2014. Proposal for an international molybdenum isotope measurement standard and
701 data representation. Geostand. Geoanal. Res. 38, 149–151. https://doi.org/10.1111/j.1751-
702 908X.2013.00275.x
703 Neubert, N., Nägler, T.F., Böttcher, M.E., 2008. Sulfidity controls molybdenum isotope fractionation
704 onto euxinic sediments: Evidence from the modern Black Sea. Geology 36, 775–778.
705 https://doi.org/10.1130/G24959A.1
706 Noordmann, J., Weyer, S., Montoya-Pino, C., Dellwig, O., Neubert, N., Eckert, S., Paetzel, M.,
707 Böttcher, M., 2015. Uranium and molybdenum isotope systematics in modern euxinic basins:
708 Case studies from the central Baltic Sea and the Kyllaren fjord (Norway). Chem Geol, 396, 182–
709 195. https://doi.org/10.1016/j.chemgeo.2014.12.012
710 Pan, W., Cao, M., Du, Y., Cheng, M., Zhou, Y.-Q., Algeo, T.J., Zhao, M.-Y., Thibault, N., Li, C., Wei,
711 G.-Y., Dahl, T.W., 2021. Paired U and Mo isotope evidence for pervasive anoxia in the
712 Cryogenian early interglacial ocean. Precambrian Res. 361, 106244.

https://doi.org/10.1016/j.precamres.2021.106244

Peng, X., Zhu, X.-K., Shi, F., Yan, B., Zhang, F., Zhao, N., Peng, P., Li, J., Wang, D., Shields, G.A., 2019. A deep marine organic carbon reservoir in the non-glacial Cryogenian ocean (Nanhua Basin, South China) revealed by organic carbon isotopes. Precambrian Res. 321, 212–220. https://doi.org/10.1016/j.precamres.2018.12.013

Poulton, S.W., Canfield, D.E., 2005. Development of a sequential extraction procedure for iron: implications for iron partitioning in continentally derived particulates. Chem. Geol. 214, 209–221. https://doi.org/10.1016/j.chemgeo.2004.09.003

Poulton, S.W., Canfield, D.E., 2011. Ferruginous conditions: A dominant feature of the ocean through Earth's history. Elements 7, 107–112. https://doi.org/10.2113/gselements.7.2.107

Poulton, S.W., 2021. The Iron Speciation Paleoredox Proxy. Cambridge University Press. Cambridge, United Kingdom. https://doi.org/10.1017/9781108847148

Poulson, R.L., Siebert, C., McManus, J., Berelson, W.M., 2006. Authigenic molybdenum isotope signatures in marine sediments. Geology 34, 617–620. https://doi.org/10.1130/G22485.1

Poulson Brucker, R.L., McManus, J., Severmann, S., Berelson, W.M., 2009. Molybdenum behavior during early diagenesis: insights from Mo isotopes. Geochem. Geophys. Geosyst. 10, Q06010. https://doi.org/10.1029/2008GC002180

Poulson, Brucker R.L., McManus, J., Poulton, S.W., 2012. Molybdenum isotope fractionations observed under anoxic experimental conditions. Geochemical Journal 46, 201–209. https://doi.org/10.2343/geochemj.1.0167

Prave, A.R., Condon, D.J., Hoffmann, K.H., Tapster, S., Fallick, A.E., 2016. Duration and nature of the end-Cryogenian (Marinoan) glaciation. Geology 44(8), 631–634. https://doi.org/10.1130/g38089.1

Raiswell, R., Canfield, D.E., 1998. Sources of iron for pyrite formation in marine sediments. Am. J. Sci. 298, 219–245. https://doi.org/10.2475/ajs.298.3.219

Rooney, A.D., Yang, C., Condon, D.J., Zhu, M., Macdonald, F.A., 2020. U-Pb and Re-Os geochronology tracks stratigraphic condensation in the Sturtian snowball Earth aftermath. Geology 48(6), 625–629. https://doi.org/10.1130/G47246.1

Rudnick, R.L., Gao, S., 2003. Composition of the continental crust. In: Rudnick, R.L. (Ed.), The Crust. Elsevier, pp. 1–64. http://dx.doi.org/10.1016/b0-08-043751-6/03016-4

Sarmiento, J.L., Gruber, N., 2006. Ocean Biogeochemical Dynamics. Princeton University Press, New

743 Jersey, USA. https://doi.org/10.1515/9781400849079
744 Scheller, E.L., Dickson, A.J., Canfield, D.E., Korte, C., Kristiansen, K.K., Dahl, T.W., 2018. Ocean
745 redox conditions between the snowballs – Geochemical constraints from Arena Formation, East
746 Greenland. Precambrian Res. 319, 173–186. https://doi.org/10.1016/j.precamres.2017.12.009
747 Scott, C., Lyons, T.W., Bekker, A., Shen, Y., Poulton, S.W., Chu, X., Anbar, A.D., 2008. Tracing the
748 stepwise oxygenation of the Proterozoic ocean. Nature 452, 456–459.
749 https://doi.org/10.1038/nature06811
750 Scholz, F., Baum, M., Siebert, C., Eroglu, S., Dale, A., Naumann, M., Sommer, S., 2018. Sedimentary
751 molybdenum cycling in the aftermath of seawater inflow to the intermittently euxinic Gotland
752 Deep, Central Baltic Sea. Chem. Geol. 491, 27–38.
753 https://doi.org/10.1016/j.chemgeo.2018.04.031
754 Shi, F.-Q., Zhu, X.-K., Yan, B., Liu, Y.-Q., Zhang, F.-F., Zhao, N.-N., Chu, M.-K., 2016. Geochemical
755 characteristics and metallogenic mechanism of the Xiangtan manganese ore deposit in Hunan
756 Province. Acta Petrologica et Mineralogica 35, 443–456. (in Chinese with English abstract)
757 Siebert, C., Nagler, T.F., von Blanckenburg, F., Kramers, J.D., 2003. Molybdenum isotope records as a
758 potential new proxy for paleoceanography. Earth Planet. Sci. Lett. 211, 159–171.
759 https://doi.org/10.1016/S0012-821X(03)00189-4
760 Sperling, E.A., Wolock, C.J., Morgan, A.S., Gill, B.C., Kunzmann, M., Halverson, G.P., Macdonald,
761 F.A., Knoll, A.H., Johnston, D.T., 2015. Statistical analysis of iron geochemical data suggests
762 limited late Proterozoic oxygenation. Nature 523, 451–454. https://doi.org/10.1038/nature14589
763 Tan, Z., Jia, W., Li, J., Yin, L., Wang, S., Wu, J., Song, J., Peng, P.A., 2021. Geochemistry and
764 molybdenum isotopes of the basal Datangpo Formation: Implications for ocean-redox conditions
765 and organic matter accumulation during the Cryogenian interglaciation. Palaeogeogr.
766 Palaeoclimatol. Palaeoecol. 563, 110169. https://doi.org/10.1016/j.palaeo.2020.110169
767 Tasistro-Hart, A.R., Macdonald, F.A., Crowley, J.L., Schmitz, M.D., 2025. Four-million-year Marinoan
768 snowball shows multiple routes to deglaciation. PNAS 122(18), e2418281122.
769 https://doi.org/10.1073/pnas.2418281122
770 Tribovillard, N., Algeo, T.J., Lyons, T., Riboulleau, A., 2006. Trace metals as paleoredox and
771 paleoproductivity proxies: An update. Chem. Geol. 232, 12–32.
772 https://doi.org/10.1016/j.chemgeo.2006.02.012

773 Tribovillard, N., Algeo, T.J., Baudin, F., Riboulleau, A., 2012. Analysis of marine environmental
774 conditions based onmolybdenum–uranium covariation—Applications to Mesozoic
775 paleoceanography. Chem. Geol. 324–325, 46–58. https://doi.org/10.1016/j.chemgeo.2011.09.009
776 Voegelin, A.R., Pettke, T., Greber, N.D., von Niederhäusern, B., Nägler, T.F., 2014. Magma
777 differentiation fractionates Mo isotope ratios: Evidence from the Kos Plateau Tuff (Aegean Arc).
778 Lithos 190–191, 440–448. http://dx.doi.org/10.1016/j.lithos.2013.12.016
779 Wang, J., Li, Z.-X., 2003. History of Neoproterozoic rift basins in South China: implications for
780 Rodinia break-up. Precambrian Res. 122, 141–158. https://doi.org/10.1016/S0301-
781 9268(02)00209-7
782 Wang, L., Cao, M., Lin, Y.-b., Wu, F., Tang, Q., Zhang, F., 2025. Reconstruction of marine redox
783 landscape during the Cryogenian interglacial oceans using thallium isotopes. Earth and Planetary
784 Science Letters 662, 119419. https://doi.org/10.1016/j.epsl.2025.119419
785 Wang, D., Zhu, X.K., Zhao, N., Yan, B., Li, X.H., Shi, F., Zhang, F., 2019. Timing of the termination of
786 Sturtian glaciation: SIMS U-Pb zircon dating from South China. J. Asian Earth Sci. 177, 287–294.
787 https://doi.org/10.1016/j.jseaes.2019.03.015
788 Wei, W., Yu, W., Du, Y., Algeo, T.J., Li, Z., Cheng, M., Wang, P., Zhang, J., Robbins, L.J., Konhauser,
789 K., 2024. A new salinity-based model for Cryogenian Mn-carbonate deposits. Precambrian
790 Research 403, 107309. https://doi.org/10.1016/j.precamres.2024.107309
791 Xiao, S., Tang, Q., 2018. After the boring billion and before the freezing millions: evolutionary patterns
792 and innovations in the Tonian Period. Emerg Top Life Sci. 2, 161–171.
793 https://doi.org/10.1042/ETLS20170165
794 Ye, Y., Wang, H., Zhai, L., Wang, X., Wu, C., Zhang, S., 2018. Contrasting Mo–U enrichments of the
795 basal Datangpo Formation in South China: Implications for the Cryogenian interglacial ocean
796 redox. Precambrian Res. 315, 66–74. https://doi.org/10.1016/j.precamres.2018.07.013
797 Zhang, F., Zhu, X., Yan, B., Kendall, B., Peng, X., Li, J., Algeo, T.J., Romaniello, S., 2015.
798 Oxygenation of a Cryogenian ocean (Nanhua Basin, South China) revealed by pyrite Fe isotope
799 compositions. Earth Planet. Sci. Lett. 429, 11–19. http://dx.doi.org/10.1016/j.epsl.2015.07.021
800 Zhang, Q.-R., Li, X.-H., Feng, L.-J., Huang, J., Song, B., 2008. A new age constraint on the onset of
801 the Neoproterozoic glaciations in the Yangtze Platform, South China. J. Geol. 116, 423–429.
802 https://doi.org/10.1086/589312

803 Zhou, C.M., Huyskens, M.H., Xiao, S., Yin, Q.Z., 2020. Refining the termination age of the
804 Cryogenian Sturtian glaciation in South China. Palaeoworld 29, 462–468.
805 https://doi.org/10.1016/j.palwor.2020.04.002
806 Zhu, M., Zhang, J., Yang, A., 2007. Integrated Ediacaran (Sinian) chronostratigraphy of South China.
807 Palaeogeogr. Palaeoclimatol. Palaeoecol. 254, 7–61. https://doi.org/10.1016/j.palaeo.2007.03.025
808 Zhu, S., Zhu, M., Knoll, A.H., Yin, Z., Zhao, F., Sun, S., Qu, Y., Shi, M., Liu, H., 2016. Decimetre-
809 scale multicellular eukaryotes from the 1.56-billion-year-old Gaoyuzhuang Formation in North
810 China. Nature Communications 7(1), 11500. https://doi.org/10.1038/ncomms11500